









Cite this: *Nanoscale*, 2018, **10**, 18642

## Ultra-high performance flexible piezopotential gated $\text{In}_{1-x}\text{Sn}_x\text{Se}$ phototransistor†

Christy Roshini Paul Inbaraj,  <sup>a,b,c</sup> Roshan Jesus Mathew,  <sup>a,b,d</sup> Golam Haider,  <sup>c</sup> Tzu-Pei Chen, <sup>b,c</sup> Rajesh Kumar Ulaganathan, <sup>e</sup> Raman Sankar,  <sup>e,f</sup> Krishna Prasad Bera, <sup>b,c</sup> Yu-Ming Liao, <sup>b,c</sup> Monika Kataria, <sup>d,g,h</sup> Hung-I Lin, <sup>c</sup> Fang Cheng Chou, <sup>e</sup> Yit-Tsong Chen,  <sup>d,i</sup> Chih-Hao Lee  <sup>a</sup> and Yang-Fang Chen\*<sup>c</sup>

Flexible optoelectronic devices facilitated by the piezotronic effect have important applications in the near future in many different fields ranging from solid-state lighting to biomedicine. Two-dimensional materials possessing extraordinary mechanical strength and semiconducting properties are essential for realizing nanopiezotronics and piezo-phototronics. Here, we report the first demonstration of piezo-phototronic properties in  $\text{In}_{1-x}\text{Sn}_x\text{Se}$  flexible devices by applying systematic mechanical strain under photoexcitation. Interestingly, we discover that the dark current and photocurrent are increased by five times under a bending strain of 2.7% with a maximum photoresponsivity of  $1037 \text{ AW}^{-1}$ . In addition, the device can act as a strain sensor with a strain sensitivity up to 206. Based on these values, the device outperforms the same class of devices in two-dimensional materials. The underlying mechanism responsible for the discovered behavior can be interpreted in terms of piezoelectric potential gating, allowing the device to perform like a phototransistor. The strain-induced gate voltage assists in the efficient separation of photogenerated charge carriers and enhances the mobility of  $\text{In}_{1-x}\text{Sn}_x\text{Se}$ , resulting in good performance on a freeform surface. Thus, our multifunctional device is useful for the development of a variety of advanced applications and will help meet the demand of emerging technologies.

Received 28th June 2018,  
Accepted 13th September 2018

DOI: 10.1039/c8nr05234d

rsc.li/nanoscale

## Introduction

The integration of multifunctional devices in a compact system, such as the Internet of Things (IoT), has recently increased demand for functional materials that can potentially simplify the device architecture. Towards this end, tuning the properties of two-dimensional materials *via* strain engineering has recently become a popular research field due to its potential to create functional devices with a wide range of

applications.<sup>1–4</sup> Depending on the crystal structure, mechanical strain causes changes in the physical properties of a material by creating a potential called a piezoelectric potential, which can be observed in non-centrosymmetric crystals lacking inversion symmetry.<sup>1</sup> This provides additional freedom to control device performance. For example, the piezo-phototronic voltage-induced gating can be tuned by applied mechanical strain in the constituent materials. Moreover, the lattice parameters can be changed by applied strain, allowing the energy bandgap of the constituents to be tuned.

Starting with graphene, h-BN,  $\text{MoS}_2$  and  $\text{WSe}_2$  were found to possess piezoelectric properties.<sup>5–11</sup> For instance, monolayer  $\text{MoS}_2$  was experimentally shown to exhibit piezoelectricity with a piezoelectric coefficient of  $e_{11} = 2.9 \times 10^{-10} \text{ C m}^{-1}$ ,<sup>11</sup> and the piezoresistive gauge factor of  $\text{MoS}_2$  was found to be comparable with that of silicon strain sensors, demonstrating the piezoresistive property of  $\text{MoS}_2$ .<sup>10</sup> However, these piezotronic properties of  $\text{MoS}_2$  can only be realized in monolayers; these properties are diminished as additional layers are added. Fortunately, piezoelectricity has been theoretically predicted in two-dimensional group-III and group-IV monochalcogenides.<sup>5,12</sup> Owing to its low Young's modulus, strain engineering in group-III monochalcogenide InSe has attracted considerable attention.<sup>1,2</sup> InSe, which is one of the most widely studied

<sup>a</sup>Department of Engineering and System Science, National Tsing Hua University, Hsinchu 30013, Taiwan

<sup>b</sup>Nano-Science and Technology Program, Taiwan International Graduate Program, Academia Sinica, Taipei 11529, Taiwan

<sup>c</sup>Department of Physics, National Taiwan University, Taipei 10617, Taiwan.  
E-mail: yfchen@phys.ntu.edu.tw

<sup>d</sup>Institute of Atomic and Molecular Sciences, Academia Sinica, Taipei 10617, Taiwan  
<sup>e</sup>Center for Condensed Matter Sciences, National Taiwan University, Taipei 10617, Taiwan

<sup>f</sup>Institute of Physics, Academia Sinica, Taipei 11529, Taiwan

<sup>g</sup>Department of Physics, National Central University, Chung-Li 320, Taiwan

<sup>h</sup>Molecular Science and Technology Program, Taiwan International Graduate Program, Academia Sinica, Taipei 11529, Taiwan

<sup>i</sup>Department of Chemistry, National Taiwan University, Taipei, 10617, Taiwan

† Electronic supplementary information (ESI) available. See DOI: 10.1039/c8nr05234d

monochalcogenides, has high carrier mobility and external quantum efficiency in few-layered films.<sup>13,14</sup> On the other hand, *ab initio* calculations of InSe reveal that the  $\epsilon$ ,  $\gamma$  and  $\beta$  phase is non-centrosymmetric in bulk, few layer and odd number of layers respectively,<sup>15</sup> making it a good candidate for piezotronic devices. To the best of our knowledge, no study has used the piezoelectric, semiconducting and photo-excitation properties of InSe to develop piezo-phototronic effect-assisted flexible optoelectronic devices.

The present work is mainly focused on demonstrating piezoelectric effects in group-III monochalcogenide InSe and its effects on piezopotential gating in flexible optoelectronic devices with the goal of achieving high-performance photodetection. To increase the conductivity of the material *via* electron concentration and obtain a large difference in current under applied strain, Sn is doped into InSe.<sup>16</sup> Moreover, doping up to 1% Sn into InSe has been shown to increase the mobility of the material,<sup>17</sup> thereby improving device performance. Hence, this study focuses on 1% Sn-doped InSe single crystals. We demonstrate the piezo-phototronic effect in a Sn-doped InSe flexible phototransistor fabricated on a polyimide substrate. Interestingly, we found that the dark current and photocurrent of the device can be tuned by applying external tensile strain, and the obtained device performance exceeds those reported for flexible photodetectors based on two-dimensional materials.<sup>18</sup> Similarly, the gauge factor of the Sn-doped InSe strain sensor is comparable with the best value reported for the same class of devices.<sup>10</sup> The underlying mechanism of the enhanced optoelectronic properties can be understood based on the strain-induced changes in band structure and piezoelectric gating in the photogenerated carriers.

## Results and discussion

Sn-Doped InSe single crystal ( $\text{In}_{1-x}\text{Sn}_x\text{Se}$ ) was grown using the Bridgman technique by adding 1% Sn to replace In atoms ( $\text{In}_{0.9}\text{Sn}_{0.1}\text{Se}$ , hereafter referred to as InSnSe), as detailed in the Experimental section. The  $\gamma$ -rhombohedral InSnSe single crystal has a layered structure with a hexagonal lattice (Fig. 1a) similar to that of InSe, making it feasible for mechanical exfoliation.

The X-ray diffraction (XRD) pattern of the InSnSe single crystal (Fig. 1b) is indexed to InSe with a rhombohedral structure with lattice constants  $a = b = 4.00 \text{ \AA}$  and  $c = 24.94 \text{ \AA}$  (JCPDS PDF no. 71-0447). The prominent diffraction peaks at  $11.01^\circ$ ,  $21.68^\circ$ ,  $31.50^\circ$ ,  $32.58^\circ$ ,  $43.9^\circ$  and  $67.88^\circ$  can be ascribed to the (003), (006), (015), (009), (0012) and (0018) planes of InSnSe, respectively. The peak shift observed for InSnSe compared to InSe (JCPDS PDF No. 71-0447) is attributed to Sn doping, which causes changes in the inter-planar spacing of the crystal. The strong diffraction peak at  $31.5^\circ$  confirms the rhombohedral phase of the  $\gamma$ -InSnSe crystal. The presence of In, Sn and Se elements and their uniform distribution were confirmed with field-emission scanning electron microscopy (FE-SEM) equipped with energy-dispersive X-ray spectroscopy (EDAX), as shown in Fig. S1.† The InSnSe single crystals were mechanically exfoliated to obtain few-layered flakes and transferred using PDMS to a flexible polyimide adhered to a polyethylene terephthalate (PET) substrate. An atomic force microscopy (AFM) image of an exfoliated InSnSe single crystal is shown in Fig. 1c. The inset shows the height profile representing a layer thickness of  $\approx 17 \text{ nm}$ .

Fig. 2a shows a schematic illustration of the few-layered InSnSe device. The electrical contacts were formed *via* the thermal evaporation of Cr/Au (7/70 nm) using a shadow masking technique. The channel length was found to be approximately  $12.57 \mu\text{m}$ . The optical microscopy image of the real device is shown in the inset of Fig. 2a. To evaluate the InSnSe device as a photodetector, the electrical transport properties were measured under different fluencies of a 633 nm laser, as shown in Fig. 2b. The drain-source current remained slightly non-linear without any saturation until the maximum applied drain bias of 10 V in the laser illumination intensity range of  $7.021 \mu\text{W cm}^{-2}$  to  $20.2 \text{ mW cm}^{-2}$  (Fig. 2b). For a detailed investigation, the photocurrent generated ( $I_{\text{ph}} = I_{\text{light}} - I_{\text{dark}}$ ) at  $V_{\text{ds}} = 10 \text{ V}$  is plotted as a function of laser power illumination (Fig. 2c) and fitted with the power law  $I_{\text{ph}} \propto P^\alpha$ , where  $\alpha \approx 0.37$ . The deviation of  $\alpha$  from the optimal value of 1 validates the sublinear behavior of photoresponse.<sup>19</sup> This type of sublinear power dependence is associated with the interfacial trap states between InSnSe and polyimide.<sup>19</sup> The high photocurrent obtained at high drain-source voltage is due to the

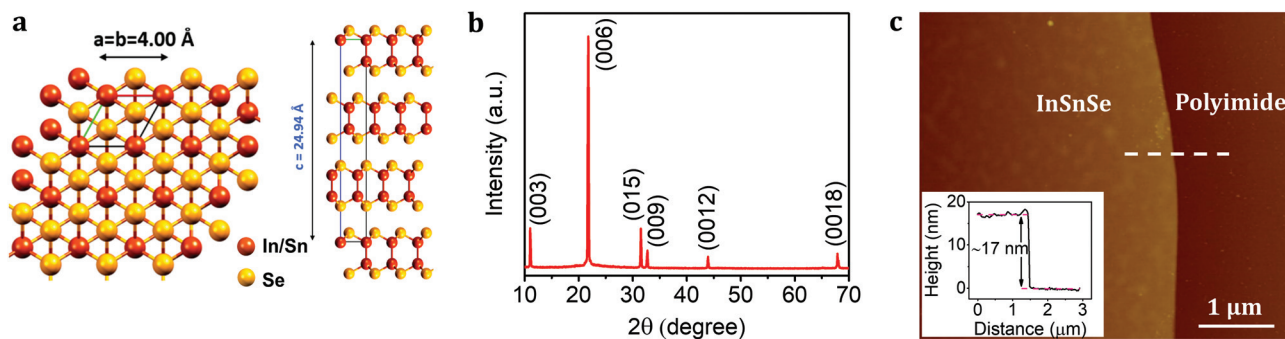


**Fig. 1** Characterization of an InSnSe crystal: (a) crystal structure and lattice parameters of InSnSe single crystal; (b) X-ray diffraction pattern of InSnSe single crystal; and (c) atomic force microscopy image and height profile of the exfoliated InSnSe flakes.

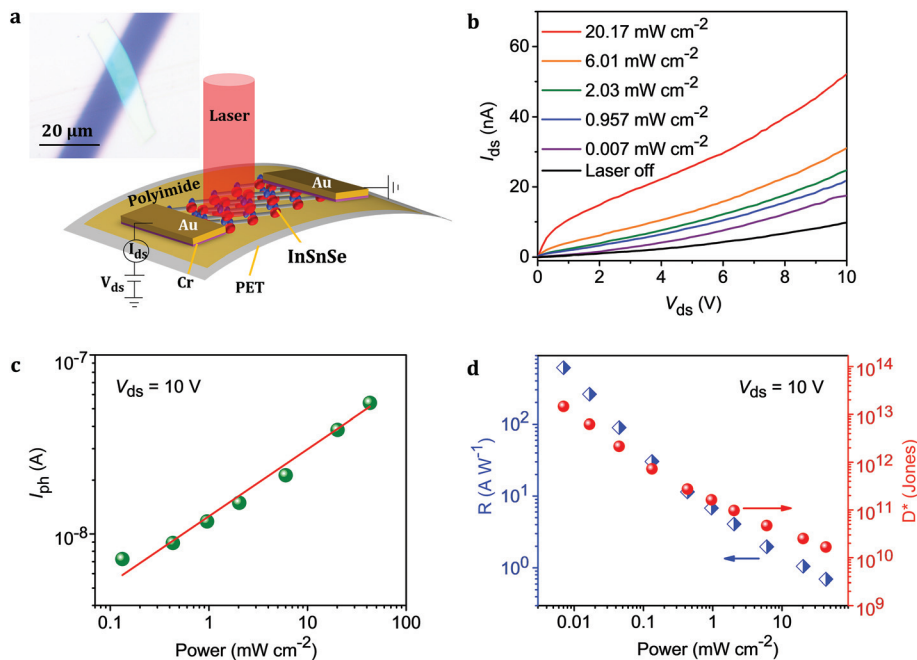


**Fig. 2** Device characteristics in the planar state. (a) Schematic representation of the few-layered InSnSe photodetector. (b)  $I_{ds}$ - $V_{ds}$  characteristic curve of the photodetector measured in the dark at different laser power intensities. (c) Photocurrent generated at  $V_{ds} = 10$  V as a function of illuminated laser power intensity. (d) Photoresponsivity ( $R$ ) and detectivity ( $D^*$ ) at  $V_{ds} = 10$  V as functions of laser power intensity.

enhanced drift velocity at high bias voltage, which potentially reduces the carrier transit time  $\tau_t$  and decreases electron-hole recombination.<sup>20</sup> The responsivity ( $R$ ) of the device was determined by  $R = I_{ph}/PS$ , where  $I_{ph}$  is the generated photocurrent,  $P$  is the laser power intensity, and  $S$  is the illuminated area of the device.<sup>18</sup> Similarly, the detectivity ( $D^*$ ) of the photodetector is an important parameter for assessing the device sensitivity.  $D^*$  is inversely related to the noise equivalent power (NEP), which quantifies the minimum optical power that a photodetector can differentiate from noise.<sup>21</sup> As the shot noise in the dark current contributes significantly to noise in the photodetector, the detectivity was determined as  $D^* = RS^{1/2}/(2eI_{dark})^{1/2}$ , where  $R$  is the photoresponsivity,  $S$  is the effective area,  $e$  is the electronic charge, and  $I_{dark}$  is the dark current. The input laser intensity dependences of the photoresponsivity and detectivity (at  $V_{ds} = 10$  V) of the device are depicted in Fig. 2d. The decrease in responsivity with increasing laser power density is attributed to the fact that the increase in carrier density with more intense laser power can boost the recombination rate or carrier scattering.<sup>21</sup> The maximum responsivity attained without strain at  $7.021 \mu\text{W cm}^{-2}$  laser power is  $609 \text{ A W}^{-1}$ , which is two orders of magnitude higher than that reported for an InSe photodetector on a PET substrate.<sup>18</sup> This is because doping with Sn enhanced the carrier mobility in the InSnSe single crystal.<sup>16</sup> Consequently, the decreased carrier transit time enhanced the responsivity, as discussed earlier. The maximum photodetectivity at a laser power of  $7.021 \mu\text{W cm}^{-2}$  is  $1.30 \times 10^{13}$  Jones, which is comparable to those of previously reported photodetectors based on 2D materials.<sup>18,22,23</sup> First, the photodetectivity indicates that the shot noise from the dark current

greatly affects the device performance. Second, the higher detectivity estimated for the InSnSe device indicates a lower NEP value, signifying a better photodetecting performance of the device.

The photogain ( $\eta$ ) of a detector is defined as the number of electrons detected per incident photon and can be expressed as  $\eta = Rhc/e\lambda$ , where  $R$  again is the photoresponsivity,  $h$  is Planck's constant,  $c$  is the speed of light, and  $\lambda$  is the wavelength of the incident light. Fig. S2a† depicts the photogain of the detector as a function of laser power intensity. The maximum photogain obtained at the lowest laser power is  $\eta = 1195$ . The transient photoresponse of the photodetector at  $V_{ds} = 1$  V is obtained by sequential illumination with a 633 nm laser ( $132.5 \mu\text{W cm}^{-2}$ ), as shown in Fig. S2b.† The consistent performance of the device over the extended period of laser illumination demonstrates the stability of the device. The response time and recovery time of the device were found to be less than 0.23 and 0.24 s, respectively (Fig. S2c and d†), and were limited by the response time of the measurement setup. The enhancement in current due to the InSnSe layer is depicted in Fig. S3.†

To demonstrate the device as a piezopotential gated phototransistor, we mechanically bent the device. The bending induces a uniaxial mechanical bending strain ( $\epsilon$ ) on the device, which can be calculated by  $\epsilon = (t/2R_c) \times 100\%$ , where  $t$  is the thickness of the substrate, and  $R_c$  is the radius of curvature (Fig. S4†).<sup>24</sup> The device performance under bending strain is shown in Fig. 3. The  $I_{ds}$ - $V_{ds}$  plot of the device in dark conditions under different strains up to 2.7% is shown in Fig. 3a. This plot shows an increase in drain-source current with

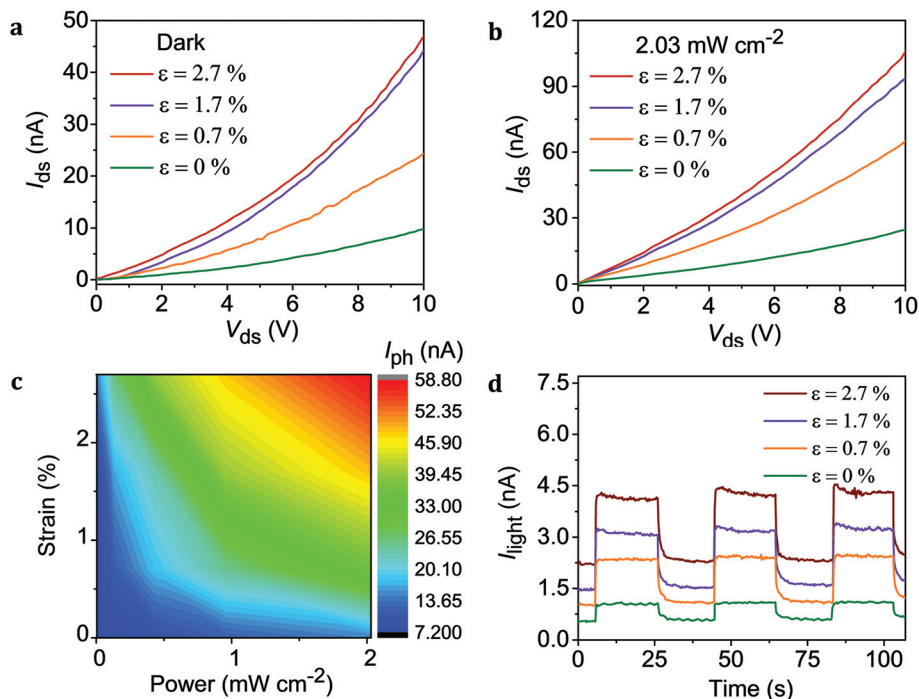


**Fig. 3** Device characteristics in the bending state. (a) and (b)  $I_{ds}$ - $V_{ds}$  curves measured at different strains under dark and laser-illuminated conditions, respectively. (c) Contour plot showing the generated photocurrent as functions of strain and laser power intensity. (d) Photo-switching characteristics of the device under different strain conditions with an illuminated laser power intensity of  $132.48 \mu\text{W cm}^{-2}$  at  $V_{ds} = 1 \text{ V}$ .

applied strain. Analogous trend was realized under the laser illumination of constant laser power at different applied strains as shown in Fig. 3b. The dependence of drain-source current on simultaneous variation of input laser power density and applied bending strain is depicted in Fig. S5.† Similarly, the photocurrent generated ( $I_{ph} = I_{light} - I_{dark}$ ) on the systematic variation of applied laser power density and bending strain are depicted in Fig. S6.† Interestingly, upon the application of 2.7% strain and a power density of  $2.03 \text{ mW cm}^{-2}$ , the photocurrent is enhanced five-fold from  $\sim 15 \text{ nA}$  (0% strain) to  $60 \text{ nA}$  (2.7% strain) at  $V_{ds} = 10 \text{ V}$  (Fig. S6d†). Under the same conditions, the drain-source current increased from 20 to  $100 \text{ nA}$  at  $10 \text{ V}$ , which is also a nearly five-fold increase. To make the observations more clear, a contour plot showing the photocurrent as functions of strain and laser power density is shown in Fig. 3c. This figure indicates that the photocurrent increases with bending strain and laser power density. A maximum photocurrent of  $\sim 60 \text{ nA}$  is observed at an illumination of  $2.03 \text{ mW cm}^{-2}$  and 2.7% strain. The photo-switching characteristics of the device under different bending strains, at constant illumination power density of  $132.5 \mu\text{W cm}^{-2}$  and  $V_{ds} = 1 \text{ V}$  are shown in Fig. 3d. The results indicate that the device is very stable, even in strained conditions, and both the dark current and photocurrent increase with increasing strain, consistent with the contour plot in Fig. 3c. Accordingly, the responsivity of the photodetector increases from 609 to  $1037 \text{ AW}^{-1}$  at the maximum applied strain and the lowest applied laser power of  $7.021 \mu\text{W cm}^{-2}$ ; this responsivity is

twice that of the unstrained device (Fig. S5b†). The responsivity and detectivity of the photodetector under different strains are plotted as functions of laser power intensity in Fig. S7.† Similarly, the variation in photogain with mechanical strain is presented in Fig. S8.†

The effect of applied bending strain on device performance while keeping all other parameters fixed is summarized in Fig. 4. Fig. 4a and b depict the tunability of source-to-drain current at  $V_{ds} = 10 \text{ V}$  and photoresponsivity, photogain at  $V_{ds} = 10 \text{ V}$  under illumination at a laser power density of  $7.021 \mu\text{W cm}^{-2}$ , respectively. The observed phenomena can be understood as follows. The bending strain causes uniaxial strain in the lattice, which reduces the value of the exchange integral between the neighboring atoms in the crystal. As a result, the bandgap value decreases, which directly reduces the Schottky barrier height at the InSnSe/metal junction. This results in a reduction in magnitude of the overall device resistance.<sup>10</sup> Thus, the device current increases under strain. The energy band diagrams of the InSnSe device under different conditions are shown in Fig. 4c-f. At equilibrium, without voltage bias, a small Schottky barrier ( $\phi_B$ ) exists in the device (Fig. 4c). When drain-source voltage is applied, a small dark current flows, overcoming the Schottky barrier (Fig. 4d). Under laser illumination, the photogenerated carriers (electrons and holes) flow in the opposite direction due to the applied drain bias, giving rise to photocurrent (Fig. 4e). When mechanical strain is applied, the Schottky barrier height is decreased due to changes in the band



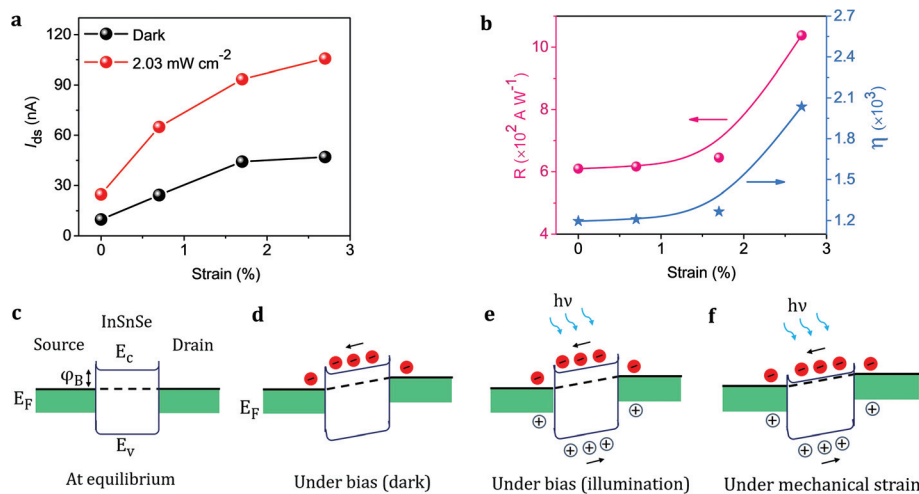


**Fig. 4** Energy band diagrams. (a) Drain–source current observed at  $V_{ds} = 10$  V as a function of strain. (b) Responsivity ( $R$ ) and photogain ( $\eta$ ) of the photodetector as a function of strain at a laser power intensity of  $7.021 \mu\text{W cm}^{-2}$  and  $V_{ds} = 10$  V. (c) Band diagram of the InSnSe device at equilibrium where  $\phi_B$  is the Schottky barrier height,  $E_F$  is the Fermi energy level,  $E_c$  is the conduction band minimum, and  $E_v$  is the valence band maximum. (d) Representation of the flow of electrons when a voltage bias is applied under dark conditions. (e) Flow of photocurrent under laser illumination. (f) Reduction in Schottky barrier height upon the application of mechanical strain.

structure of InSnSe, leading to enhanced current flow (Fig. 4f).

Similarly, when the device is bent, the upper layers of the InSnSe flakes experience tensile strain, while compressive strain persists in the lower layers. This induces charge asymmetry in the structure, which leads to a displacement of the charge center and creates a dipole moment. Altogether, a piezoelectric potential is formed due to the accretion of dipole moments from all the unit cells of a crystal.<sup>25</sup> The piezoelectric potential acts as an additional bias similar to a gate to reduce the carrier transit time. This retards electron–hole recombination and provides an applied bias voltage, resulting in more detection of photogenerated charges. Thus, along with lower device resistance, the piezoelectric potential under bending gives rise to a consistent enhancement in photocurrent with bending strain. The photoresponsivity, photocurrent gain, and detectivity are correspondingly enhanced with bending strain. These remarkable behaviors indicate that the InSnSe photodetector is very sensitive under mechanical strain, and the device functions as a phototransistor with the strain-assisted piezoelectric potential acting as the gate.

The close observation of device characteristics under mechanical strain confirms the extreme sensitivity of the device to applied strain. Therefore, the InSnSe device also acts as a strain sensor. The gauge factor, which is defined as the ratio of relative change in current under strain ( $\Delta I/I$ ) to the actual strain ( $\Delta \epsilon$ ) is estimated to be 206 (Fig. 5), comparable to the previously reported values for MoS<sub>2</sub> (ref. 10) and silicon.<sup>26</sup> The higher gauge factor may be associated with the lower Young's modulus of InSe crystal.<sup>2</sup>

To rationalize the above interpretation, we recorded the photoluminescence (PL) spectra of the device under different bending strains, as shown in Fig. 6a. Interestingly, we observed

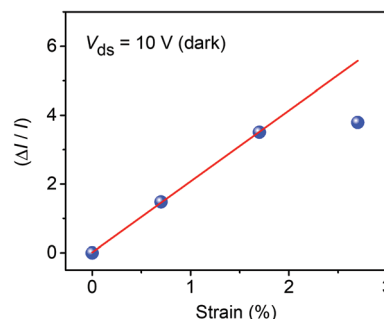


**Fig. 5** Strain sensor: relative change in current as a function of strain.

a systematic red shift in the PL peak intensity and a systematic reduction in integrated PL intensity with increasing bending strain. The bandgap energy and integrated PL intensity are shown as a function of applied bending strain in Fig. 6b. The applied strain changes the bond lengths of the constituent atoms in the unit cell. As a result, the transfer integral between the neighboring atoms changes. Thus, we observed a systematic reduction in electronic bandgap with bending strain. On the other hand, the asymmetric strain between the constituent layers modulates the charge in symmetry in the unit cells, creating strain-assisted bound charges. This creates a potential similar to the piezoelectric effect. Therefore, an intrinsic electric field is generated, which quenches the PL intensity. Although changes in the energy band dispersion of a 2D material may result in decreased PL intensity under strain, the change in PL peak energy upon strain application in this study was very small ( $\sim 0.017$  eV for 2.7% strain; Fig. 6b). However, the corresponding changes in dark current and photocurrent under strain were nearly 5–6 times (Fig. 3a and

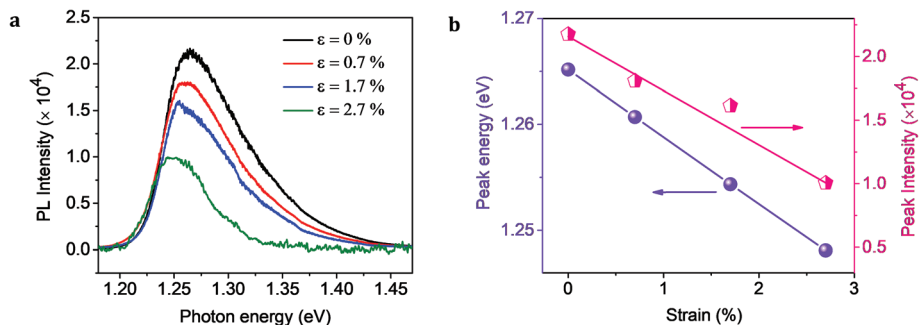


**Fig. 6** Photoluminescence spectra: (a) photoluminescence (PL) spectra of the InSnSe device measured under different strain conditions; and (b) peak energy and peak intensity of the PL spectra as functions of strain.

b). Hence, the effect of the decrease in PL intensity due to strain-modulated charge asymmetry is more dominant than the effect of the change in the energy band dispersion of the 2D material. These observations provide firm evidence to support the piezo-phototronic effect in the crystal and provide additional freedom to tune the optoelectronic performance of our design.

To support our interpretation, Raman scattering measurements were performed, and the strain-induced evolution of Raman phonon modes were investigated for the InSnSe devices in the frequency range of 80 to 250  $\text{cm}^{-1}$  (Fig. 7). In unstrained conditions ( $\epsilon = 0\%$ ), three prominent Raman peaks were observed at 110.86, 173.90 and 223.77  $\text{cm}^{-1}$ , which

can be attributed to the non-resonant Raman vibrational phonon modes  $A^1_{1g}$ ,  $E^2_{1g}$  and  $A^2_{1g}$ , respectively. The observed Raman spectra contributed by the interlayer interaction appear with a significant redshift in phonon frequency compared with that of a pure InSe crystal.<sup>27,28</sup> The inferred shifts from the reported value of pure InSe crystal<sup>27,28</sup> are  $\sim 6 \text{ cm}^{-1}$  for  $A^1_{1g}$ ,  $\sim 5 \text{ cm}^{-1}$  for  $E^2_{1g}$  and  $\sim 3 \text{ cm}^{-1}$  for  $A^2_{1g}$ , and the central maximum of each mode shifts with the same value for various applied strains. The in-phase vibration of covalently bonded In and Se accounts for the  $A_1$  phonon mode by In–In bond stretching and the E mode by In–In bond bending.<sup>29</sup> The observed peak shift in these first-order non-polar phonon modes stems from the doping of Sn into the InSe lattice,

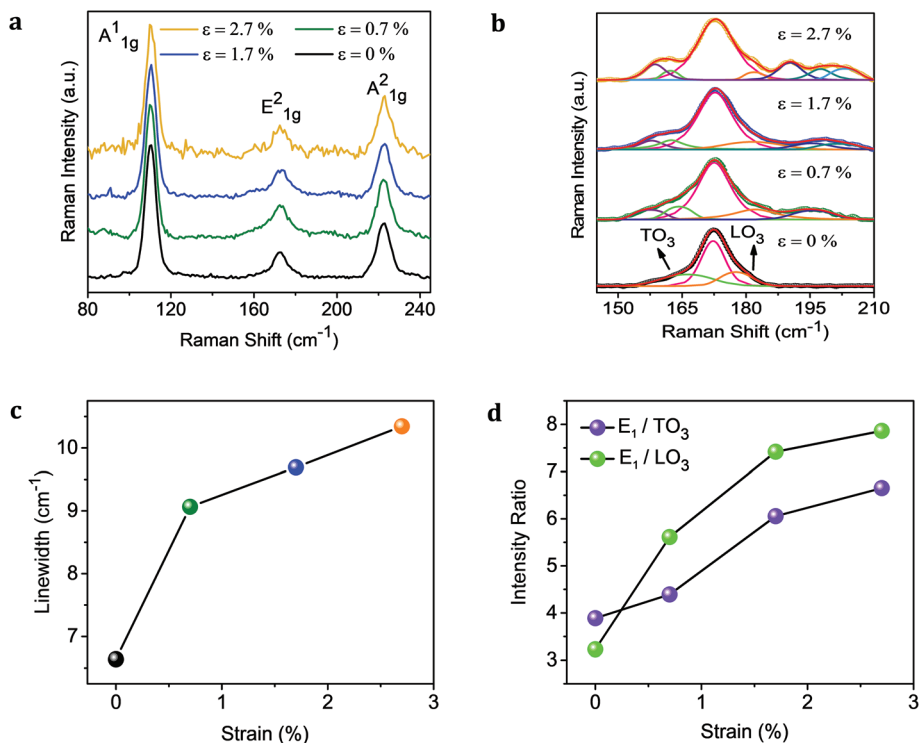


**Fig. 7** Raman spectra. (a) Raman spectra of exfoliated InSnSe flakes measured under different strain conditions. (b) Deconvoluted peaks of the  $E^2_{1g}$  phonon mode under different strains. (c) and (d) Full width at half maximum of the  $E^2_{1g}$  mode ( $\approx 172 \text{ cm}^{-1}$ ) and intensity ratio as functions of strain, respectively.

similar to the peak shift observed in GaS-doped InSe crystal system.<sup>30</sup> The effect of strain on Sn-doped InSe devices can be understood from the systematic changes in the phonon modes of the Raman spectra. The strain-induced evolution of Raman phonon modes was investigated by deconvoluting each prominent phonon mode. The spectral regions were well fit by the Gaussian/Lorentzian components. The regions displayed as modes  $A^1_{1g}$ ,  $E^2_{1g}$  and  $A^2_{1g}$  in Fig. 7a are magnified and shown with fitted data in Fig. S9a, Fig. 7b and Fig. S9b,† respectively.

### $A^1_{1g}$ phonon mode

In the planar state, the peak at  $110\text{ cm}^{-1}$  ( $A^1_{1g}$  mode) was deconvoluted into peaks at  $102$  and  $120\text{ cm}^{-1}$ . The weak Raman peaks at  $102$  and  $120\text{ cm}^{-1}$  correspond to the rigid shear  $B^3_g$  and  $A_g3$  phonon modes of SnSe<sup>31</sup> with a slight red-shift, which also confirms the incorporation of Sn in the InSe lattice with bonding to Se atoms. The same trend is observed for all four strain states without significant shifts in peak positions and line widths; slight decreases in  $A^1_{1g}/B^3_g$  and  $A^1_{1g}/A_g3$  were observed at a strain of 2.7%.

### $E^2_{1g}$ phonon mode

An analysis of the deconvoluted components of the second prominent peak ( $E^2_{1g}$  phonon mode) indicated that strain induced (a) a minor blue shift in the  $E^2_{1g}$  mode, (b) a broadening of line width in the central peak, (c) multiple splitting of the  $E^2_{1g}$  phonon mode, and (d) variation in intensity ratio between the splitted peaks. Detail of the region between  $150$  and  $210\text{ cm}^{-1}$  is presented in Fig. 7b for various applied strains. This figure indicates that the  $E^2_{1g}$  mode can be deconvoluted into three components with peaks at  $178$ ,  $172.27$  and  $166\text{ cm}^{-1}$  under zero strain. Chandrasekhar *et al.*<sup>32</sup> reported peaks at  $166$  and  $178.0\text{ cm}^{-1}$  corresponding to the  $TO_3$  and  $LO_3$  phonon frequencies of SnSe from a Kramers–Kronig analysis of infrared reflectivity. At higher strain levels, the  $E^2_{1g}$  mode shows multiple splittings that can be perfectly fit with multiple Gaussian/Lorentzian components. The central peak ( $E^2_{1g}$ ) exhibits a minor blue shift (Fig. S10†), and its full width at half maximum (FWHM) gradually increases from  $6.63\text{ cm}^{-1}$  in the planar state to  $10.34\text{ cm}^{-1}$  under an applied strain of 2.7% (Fig. 7c). The minor frequency shift results from a minimal applied external strain and can be interpreted as an internal strain-induced change in bond length of the material under applied external strain. The dependence of the vibrational frequency on the bond length  $L$  can be calculated from the relation  $L = (1.86 \times 10^5/k)^{1/3} + d$ ,<sup>33</sup> where  $k$  is the force constant. The effective mass ( $m$ ) was calculated based on the atomic weights of In and Se. The force constant can be deduced from the wavenumber according to the general relation  $\nu = \frac{1}{2\pi c} \sqrt{k/m}$ . Hence, the internal strain can be estimated from the formula  $\epsilon_{\text{int}} = \frac{\Delta L}{L_0} \times 100\%$ , where  $L_0$  is the bond length in the planar state, and  $\Delta L$  is the change in bond length under applied external strain. The calculations show

the increase in internal strain of the material from 0.05% to 0.13% proving an internal strain induced change in bond length on the application of an external strain from 0.7% to 2.7% (Table S1†). This fluctuation in bond length results in polarization, leading to the creation of dipole moment in each unit cell of the crystal. This results in the development of a piezoelectric field along the direction of applied strain. Moreover, both  $TO_3$  and  $LO_3$  phonon modes showed splitting and shifts in frequency with increasing strain. The intensity ratios between  $E^2_{1g}$  and the  $TO_3$  and  $LO_3$  modes show considerable variation as applied strain increases (*i.e.*,  $E^2_{1g}/TO_3$  gradually increases from 3.9 to 6.7, and  $E^2_{1g}/LO_3$  sharply increases from 3.2 to 7.9 as applied strain increases from 0% to 2.7%; Fig. 7d). This phenomenon is similar to the strain-induced evolution of phonon splitting and the frequency shift observed in graphene, which can be explained based on the anharmonicity of the interatomic potential of the lattice atoms.<sup>34,35</sup> The Grüneisen parameter ( $\gamma$ ) characterizes the anharmonicity of molecular potential and can be calculated by  $\gamma = -\frac{(\Delta\omega_{E^+} + \Delta\omega_{E^-})}{2\omega_E(1-\vartheta)}$ ,<sup>24</sup> where  $\omega$  is the frequency of the Raman phonon mode,  $\Delta\omega$  is the strain-induced frequency change, and  $\vartheta$  is Poisson's ratio (here,  $\vartheta$  is 0.34 for the polyimide substrate). Taking  $\Delta\omega_{E^+}$  as the frequency of the  $E^2_{1g}$  peak and  $\Delta\omega_{E^-}$  as the frequency of the  $TO_3$  peak, our calculation yielded  $|\gamma| = 1.12$  for the highest applied strain of 2.7%.

### $A^2_{1g}$ phonon mode

The deconvolution of the third prominent peak belonging to the  $A^2_{1g}$  mode gives four splitted components. The peak around  $215\text{ cm}^{-1}$  shows a blue shift in frequency with increasing applied strain. This phenomenon also can be attributed to the internal strain-induced change in bond length, resulting in polarization, as explained above. Ikari *et al.*<sup>27</sup> reported that the peak around  $215\text{ cm}^{-1}$  belongs to the LO phonon of the E mode of InSe, and the LO scattering efficiency is enhanced by the exciton–LO phonon Fröhlich interaction.

To demonstrate the wearable property of the photodetector, the electrical transport properties were evaluated by adhering polyimide tape to a pen and a nitrile glove, as shown in Fig. S11.† The recorded  $I_{\text{ds}}-V_{\text{ds}}$  characteristics of the device under dark and laser-illuminated conditions while the device was adhered to the pen are shown in Fig. S11a.† The transient photoresponse characteristics at  $V_{\text{ds}} = 1\text{ V}$  ( $P = 132.5\text{ }\mu\text{W cm}^{-2}$ ) are shown in Fig. S11b.† Similarly, the electrical transport properties and transient photoresponse characteristics of the device recorded when the device was adhered to a nitrile glove are depicted in Fig. S11c and S11d,† respectively. We also observed the piezophototronic effect in different InSnSe devices, as shown in Fig. S12.† These observations provide strong evidence for the reproducibility and repeatability of the designed devices. The variation in device performance is shown in Fig. S13.†

We stress that in addition to working as a piezopotential gated phototransistor, our multifunctional single-component

device can also act as a strain sensor. Due to the large change in current with minimal strain, the flexible characteristics of the device can be further extended to serve as a pressure sensor and a key component of electronic skins in robotics. The large quantum efficiency and piezotronic property of InSnSe provide a wide scope for designing flexible optoelectronic devices. Thus, the results of this study are very useful for realizing practical applications in the emerging area of wearable technologies.

## Conclusions

In conclusion, the piezoelectric effect in InSnSe was observed in a flexible phototransistor fabricated on a polyimide substrate. The dark current and generated photocurrent increased five-fold upon the application of strain. Our devices exhibited a photoresponsivity as high as  $1037 \text{ AW}^{-1}$  under a strain of 2.7%. Owing to the low Young's modulus, InSnSe possesses a wide tunability under low applied strain, making it an ideal candidate for high-performance strain sensors with a gauge factor of 206. The generation of piezoelectric potential, which is responsible for the underlying mechanism of enhanced photocurrent generation under applied external strain, was confirmed with the aid of photoluminescence and Raman spectroscopies. The observed piezoelectric potential of InSnSe is very useful for designing novel flexible optoelectronic devices. To illustrate the working principle, the wearable property of the device on freeform surfaces has been demonstrated. Therefore, Sn-doped InSe-based materials have wide applications in strain sensors and other functional optoelectronic devices with enhanced performance. In view of the unique flexibility of the 2D materials in this study, the findings are very useful and timely.

## Experimental section

### Growth of InSnSe single crystals

InSnSe single crystals were grown using a 99.999% pure molar mixture of Sn (1%), In and Se compounds (Sigma Aldrich). Conical quartz ampoules evacuated to  $10^{-4}$  Pa were used to synthesize  $\text{In}_{0.9}\text{Sn}_{0.1}\text{Se}$  single crystals. Homogenization of the batches followed by synthesis was carried out at 600 °C for 48 h in a horizontal furnace using the vertical Bridgman method. The ampoules and the melt were heat-treated for 24 h at 850 °C before pulling. As the melt filled the ampoule tip, the ampoule was lowered with a temperature gradient of 1 °C at a rate of  $0.1 \text{ mm h}^{-1}$ . The as-grown  $\text{In}_{0.9}\text{Sn}_{0.1}\text{Se}$  single crystals were 3 cm in length and 1.2 cm in diameter.

### Device fabrication

Few-layered InSnSe flakes were prepared by mechanically exfoliating the as-grown InSnSe single crystals using Scotch tape. The flakes were transferred to a polyimide substrate adhered to PET using PDMS for a clean transfer. The transferred

InSnSe flakes were examined using an optical microscope (Olympus, BX 51M) equipped with a charge-coupled device (CCD) (Leica, DFC495). The flake thickness was determined using AFM. A TEM copper grid was used as a shadow mask for depositing electrodes and mounted exactly on the few-layered InSnSe flakes using a custom-made micro-manipulator. A thermal evaporator was used to deposit Cr/Au electrodes with thicknesses of 7/70 nm.

### Characterization details

X-ray diffraction (XRD) analysis was used to determine the crystal structure and lattice constants with an X-ray diffractometer (Panalytical X'pert PRO) with Cu  $K\alpha$  radiation ( $\lambda = 1.540 \text{ \AA}$ ) in the  $2\theta$  range of  $5^\circ$  to  $70^\circ$  (step size =  $0.03939^\circ$ ) at room temperature. AFM was performed using a Bruker's Dimension Icon atomic force microscope. Elemental mapping was conducted with FE-SEM (Jeol JSM-7800F) equipped with EDAX (Oxford systems). Electrical measurements were performed with a probe station equipped with a Keithley 2400 electrometer. A He-Ne laser with a wavelength of 633 nm was used for laser illumination. Photoluminescence measurements were carried out at room temperature using a spectrometer (Jodson) equipped with a Horiba Syncernity detector. A laser with a wavelength of 532 nm (laser power = 1.35 mW and spectrometer grating =  $950 \text{ g mm}^{-1}$ ) was used for excitation. The Raman spectra of InSnSe flakes were recorded using a Jodson micro-Raman spectrometer consisting of an optical microscope (Olympus CX41) and a detector (Jobin Won Horiba S Drive-500 Syncernity). A 532 nm laser with a 1.03 mW power (grating =  $1800 \text{ g mm}^{-1}$ ) was used as the excitation source.

## Author contribution statement

C. R. P. I. designed the experiments and performed electrical and optical measurements. C. R. P. I. and R. J. M. fabricated the devices. C. R. P. I., G. H. and Y.-F. C. discussed the mechanism of the piezopotential gated phototransistor. R. J. M., T.-P. C. and Y.-T. C. performed the Raman spectroscopic measurements. R. K. U., R. S. and F. C. C. grew the InSnSe crystals. K. P. B., Y.-M. L., M. K. and H.-I. L. assisted in the electrical measurements. C. R. P. I., G. H., Y.-T. C. and C.-H. L. analyzed the data. C. R. P. I. wrote the manuscript. Y.-F. C. is the corresponding author in charge of project design, experimental data analysis and manuscript writing.

## Conflicts of interest

There are no conflicts to declare.

## Acknowledgements

This work was financially supported by the "Advanced Research Center for Green Materials Science and Technology" from The Featured Area Research Center Program within the



framework of the Higher Education Sprout Project by the Ministry of Education (107L9006) and the Ministry of Science and Technology in Taiwan (MOST 107-3017-F-002-001). P. Christy Roshini acknowledges the support of the Taiwan International Graduate Program, Institute of Physics, Academia Sinica, Taipei, Taiwan and National Tsing Hua University, Hsinchu, Taiwan.

## References

- W. Wu, L. Wang, R. Yu, Y. Liu, S. H. Wei, J. Hone and Z. L. Wang, *Adv. Mater.*, 2016, **28**, 8463.
- C. Song, F. Fan, N. Xuan, S. Huang, G. Zhang, C. Wang, Z. Sun, H. Wu and H. Yan, *ACS Appl. Mater. Interfaces*, 2018, **10**, 3994.
- H. Zou, X. Li, W. Peng, W. Wu, R. Yu, C. Wu, W. Ding, F. Hu, R. Liu, Y. Zi and Z. L. Wang, *Adv. Mater.*, 2017, **29**, 1.
- G. Haider, P. Roy, C. W. Chiang, W. C. Tan, Y. R. Liou, H. T. Chang, C. T. Liang, W. H. Shih and Y. F. Chen, *Adv. Funct. Mater.*, 2016, **26**, 620.
- W. Li and J. Li, *Nano Res.*, 2015, **8**, 3796.
- K. A. N. Duerloo, M. T. Ong and E. J. Reed, *J. Phys. Chem. Lett.*, 2012, **3**, 2871.
- J. H. Lee, J. Y. Park, E. B. Cho, T. Y. Kim, S. A. Han, T. H. Kim, Y. Liu, S. K. Kim, C. J. Roh, H. J. Yoon, H. Ryu, W. Seung, J. S. Lee, J. Lee and S. W. Kim, *Adv. Mater.*, 2017, **29**, 1.
- K. H. Michel and B. Verberck, *Phys. Status Solidi B*, 2011, **248**, 2720.
- X. Wang, H. Tian, W. Xie, Y. Shu, W. T. Mi, M. A. Mohammad, Q. Y. Xie, Y. Yang, J. Bin Xu and T. L. Ren, *NPG Asia Mater.*, 2015, **7**, e154.
- W. Wu, L. Wang, Y. Li, F. Zhang, L. Lin, S. Niu, D. Chenet, X. Zhang, Y. Hao, T. F. Heinz, J. Hone and Z. L. Wang, *Nature*, 2014, **514**, 470.
- H. Zhu, Y. Wang, J. Xiao, M. Liu, S. Xiong, Z. J. Wong, Z. Ye, Y. Ye, X. Yin and X. Zhang, *Nat. Nanotechnol.*, 2015, **10**, 151.
- R. Fei, W. Li, J. Li and L. Yang, *Appl. Phys. Lett.*, 2015, **107**, 173104.
- D. A. Bandurin, A. V. Tyurnina, G. L. Yu, A. Mishchenko, V. Zolyomi, S. V. Morozov, R. K. Kumar, R. V. Gorbachev, Z. R. Kudrynskiy, S. Pezzini, Z. D. Kovalyuk, U. Zeitler, K. S. Novoselov, A. Patane, L. Eaves, I. V. Grigorieva, V. I. Falko, A. K. Geim and Y. Cao, *Nat. Nanotechnol.*, 2017, **12**, 223.
- S. Lei, L. Ge, S. Najmaei, A. George, R. Koppera, J. Lou, M. Chhowalla, H. Yamaguchi, G. Gupta, R. Vajtai, A. D. Mohite and P. M. Ajayan, *ACS Nano*, 2014, **8**, 1263.
- D. T. Do, S. D. Mahanti and C. W. Lai, *Sci. Rep.*, 2015, **5**, 1.
- X. Hou, S. Chen, Z. Du and J. Cui, *RSC Adv.*, 2015, **5**, 102856.
- B. Marí, A. Segura and A. Chevy, *Appl. Phys. A: Solids Surf.*, 1988, **46**, 125.
- S. R. Tamalampudi, Y. Y. Lu, U. R. Kumar, R. Sankar, C. Da Liao, B. K. Moorthy, C. H. Cheng, F. C. Chou and Y. T. Chen, *Nano Lett.*, 2014, **14**, 2800.
- W. Luo, Y. Cao, P. Hu, K. Cai, Q. Feng, F. Yan, T. Yan, X. Zhang and K. Wang, *Adv. Opt. Mater.*, 2015, **3**, 1418.
- O. Lopez-Sanchez, D. Lembke, M. Kayci, A. Radenovic and A. Kis, *Nat. Nanotechnol.*, 2013, **8**, 497.
- G. Su, V. G. Hadjiev, P. E. Loya, J. Zhang, S. Lei, S. Maharjan, P. Dong, P. M. Ajayan, J. Lou and H. Peng, *Nano Lett.*, 2015, **15**, 506.
- R. B. Jacobs-Gedrim, M. Shanmugam, N. Jain, C. A. Durcan, M. T. Murphy, T. M. Murray, R. J. Matyi, R. L. Moore and B. Yu, *ACS Nano*, 2014, **8**, 514.
- W. Choi, M. Y. Cho, A. Konar, J. H. Lee, G. B. Cha, S. C. Hong, S. Kim, J. Kim, D. Jena, J. Joo and S. Kim, *Adv. Mater.*, 2012, **24**, 5832.
- H. J. Conley, B. Wang, J. I. Ziegler, R. F. Haglund, S. T. Pantelides and K. I. Bolotin, *Nano Lett.*, 2013, **13**, 3626.
- X. Han, M. Chen, C. Pan and Z. L. Wang, *J. Mater. Chem. C*, 2016, **4**, 11341.
- S. Yang and N. Lu, *Sensors*, 2013, **13**, 8577.
- T. Ikari, S. Shigetomi and K. Hashimoto, *Phys. Status Solidi B*, 1982, **111**, 477.
- T. J. Wieting and J. L. Verble, *Phys. Rev. B: Solid State*, 1972, **5**, 1473.
- J. F. Sánchez-Royo, G. Muñoz-Matutano, M. Brotons-Gisbert, J. P. Martínez-Pastor, A. Segura, A. Cantarero, R. Mata, J. Canet-Ferrer, G. Tobias, E. Canadell, J. Marques-Hueso and B. D. Gerard, *Nano Res.*, 2014, **7**, 1556.
- M. Zolfaghari, K. P. Jain, H. S. Mavi, M. Balkanski, C. Julien and A. Chevy, *Mater. Sci. Eng., B*, 1996, **38**, 161.
- S. Zhao, H. Wang, Y. Zhou, L. Liao, Y. Jiang, X. Yang, G. Chen, M. Lin, Y. Wang, H. Peng and Z. Liu, *Nano Res.*, 2015, **8**, 288.
- H. R. Chandrasekhar, R. G. Humphreys, U. Zwick and M. Cardona, *Phys. Rev. B: Solid State*, 1977, **15**, 2177.
- R. M. Badger, *J. Chem. Phys.*, 1934, **2**, 128.
- M. Huang, H. Yan, C. Chen, D. Song, T. F. Heinz and J. Hone, *Proc. Natl. Acad. Sci. U. S. A.*, 2009, **106**, 7304.
- O. Frank, M. Mohr, J. Maultzsch, C. Thomsen, I. Riaz, R. Jalil, K. S. Novoselov, G. Tsoukleri, J. Parthenios, K. Papagelis, L. Kavan and C. Galiotis, *ACS Nano*, 2011, **5**, 2231.